

Seasonal tracer subduction in the Subpolar North Atlantic driven by submesoscale fronts

Théo Picard¹, Jonathan Gula^{2,3}, Clément Vic², Laurent Mémery¹

¹Univ Brest, CNRS, IRD, Ifremer, Laboratoire des Sciences de l'Environnement Marin (LEMAR), IUEM,

Plouzané, France

²Univ Brest, CNRS, IRD, Ifremer, Laboratoire d'Océanographie Physique et Spatiale (LOPS), IUEM,

Plouzané, France

³Institut Universitaire de France (IUF), Paris, France

Key Points:

- Surface strain and vorticity criteria can be used to identify submesoscale fronts.
- The submesoscale fronts contribute to $\sim 40\%$ of the total tracer vertical advection subduction in winter, and less than 1% in summer.
- The tracer depth injection correlates with the surface fraction of fronts, regardless of the mixed layer depth evolution.

15 **Abstract**

16 Submesoscale flows (0.1 - 10 km) are often associated with large vertical velocities, which
 17 can have a significant impact on the transport of surface tracers, such as carbon. How-
 18 ever, global models do not adequately account for these small-scale effects, which still
 19 require a proper parameterization. In this study, we introduced a passive tracer into the
 20 surface mixed layer of a northern Atlantic Ocean simulation based on the primitive-equation
 21 model CROCO, with a horizontal resolution of $\Delta x = 800$ m, aiming to investigate the
 22 seasonal submesoscale effects on vertical transport. Using surface vorticity and strain
 23 rate criteria, we identified regions with submesoscale fronts and quantified the associ-
 24 ated subduction, that is the export of tracer below the mixed layer depth. The results
 25 suggest that the tracer vertical distribution and the contribution of frontal subduction
 26 can be estimated from surface strain and vorticity. Notably, we observed significant sea-
 27 sonal variations. In winter, the submesoscale fronts contribute up to 40% of the total
 28 vertical advective transport of tracer below the mixed layer, while representing only 5%
 29 of the domain. Conversely, in summer, fronts account for less than 1% of the domain and
 30 do not contribute significantly to the transport below the mixed layer. The findings of
 31 this study contribute to a better understanding of the seasonal water subduction due to
 32 fronts in the region.

33 **Plain Language Summary**

34 Oceanic fronts are dynamical structures characterized by enhanced gradients of vari-
 35 ables such as temperature or density. These structures are prominent and ubiquitous at
 36 the ocean surface and can reach particularly small scales, down to a few kilometers. They
 37 are known to play an important role in the vertical exchange of carbon, nutrients or heat
 38 between the surface and the ocean interior. Due to their small scale and short lifecycle,
 39 they have not been extensively sampled and a systematic quantification of their impact
 40 is missing. In this study, we set up a numerical simulation of the ocean circulation in the
 41 North Atlantic that resolves small-scale fronts. We release a tracer in upper layer of the
 42 ocean and analyse how it is transported at depth. Using criteria based on the flow ve-
 43 locity, we quantify the fraction of the ocean surface covered by fronts. We find that the
 44 average depth at which the tracer is injected depends on the prevalence of fronts, which
 45 itself shows a strong seasonality. In winter, fronts cover less than 5% of the surface area,
 46 but contribute up to 40% of the tracer vertical transport. Conversely, in summer, fronts
 47 cover less than 1% of the area and have no significant effect on tracer vertical transport.
 48 This study helps to better understand the seasonal role of fronts in vertical water trans-
 49 port. This paves the way for addressing questions related to how tracers such as carbon
 50 are distributed in the world's oceans.

51 **1 Introduction**

52 There is a growing set of evidence that submesoscale physical processes matter for
 53 the transport of oceanic tracers such as heat, carbon and nutrients (Klein & Lapeyre,
 54 2009; Omard et al., 2015; Stukel et al., 2017; Llort et al., 2018; Lévy et al., 2018; Boyd
 55 et al., 2019; Lacour et al., 2019). Submesoscale phenomena are characterised by frontal
 56 and filamentary structures with lateral scales ranging from 0.1 to 10 km. These struc-
 57 tures typically arise from baroclinic instability at the ocean surface, exhibiting Rossby
 58 ($Ro = \zeta/f$) numbers on the order of 1 (Lévy et al., 2024). Frontogenesis, responsible
 59 for ageostrophic flow patterns known as secondary circulation, induces strong and deep
 60 vertical velocities localised precisely at fronts (McWilliams, 2021; Gula, Taylor, et al.,
 61 2021). Fronts are characterised by a dense cyclonic side with downward velocities and
 62 a light anticyclonic side with upward velocities. In the context of the carbon cycle, this
 63 results in a double contribution : On the one hand, it drives nutrients, essential for the
 64 primary production, from the (interior) twilight zone into the euphotic layer (Lapeyre

& Klein, 2006; Lévy et al., 2018; Mahadevan, 2016). On the other hand, it facilitates the subduction of surface carbon (transport below the mixed layer) along isopycnal pathways, effectively storing it for extended periods (Wenegrat et al., 2020; Mahadevan et al., 2020; Freilich & Mahadevan, 2021). Furthermore, fronts actively participate in the upward heat transport from the ocean interior to the surface and are essential ingredients of the Earth's heat budget (Siegelman et al., 2020).

While it is clear that fronts play a significant role in tracer budgets, the vertical transport induced by submesoscale processes remains unresolved and is not yet parameterized in climate models (Bopp et al., 2013; Mahadevan et al., 2020). Overcoming this challenge is one of the major hurdles in ocean modeling (Fox-Kemper et al., 2019). However, although there has been recent interest in quantifying the submesoscale contribution to tracer transport, there is still no clear consensus on its impact. A major obstacle is the difficulty of sampling submesoscale processes using remote sensing and in situ observational instruments. Indeed, satellite altimetry can only detect structures larger than 100 kilometers (Chelton et al., 2011), and the measurement of vertical transport due to small-scale phenomena in the ocean remains a challenge (Mahadevan et al., 2020). The computation of submesoscale velocity gradient generally requires multiple ships, autonomous underwater vehicles, or surface drifters (Shcherbina et al., 2013; Gula, Taylor, et al., 2021). With respect to numerical simulations, it has been shown that fine-scale ocean regional circulation models with subkilometer horizontal grid spacing can accurately capture submesoscale dynamics (Mahadevan & Tandon, 2006; Capet et al., 2008; Pietri et al., 2021). However, high-resolution modeling is constrained by computational costs (Lévy et al., 2024), resulting in spatial limitations and/or idealized setups.

Various methodologies have been proposed to estimate the frontal contribution to vertical exchanges, particularly in the context of carbon export. Balwada et al. (2018) estimated that the subduction could be doubled by comparing models with 20 and 1 km horizontal resolution. Uchida et al. (2019) quantified the ageostrophic contribution using spectral analysis and found that submesoscale structures could account for about a third of the total fluxes. In Freilich and Mahadevan (2021), Lagrangian particles were used to identify particles trapped in submesoscale structures. Their findings showed that 7.7% of the particles are subducted from the mixed layer, with subduction occurring mainly in localized regions along fronts. Based on glider observations during the North Atlantic bloom and supported by numerical modeling, Omand et al. (2015) showed that submesoscale structures can contribute up to half of the total spring export of particulate organic carbon (POC). In a recent study, Balwada et al. (2021) used Joint Probability Density Function (JPDF) of surface vorticity and strain rate on an idealized fine-scale model of the Antarctic Circumpolar Current to identify fronts. They showed that submesoscale fronts, although occupying only about 5% of the surface domain, could potentially account for up to 20% of the vertical transport at the Mixed Layer Depth (MLD). This wide range of results underlines the complexity and considerable uncertainties associated with this topic.

Despite this growing body of literature, there is a notable gap in knowledge as most studies tend to overlook the seasonal variability of these phenomena. However, it is now clear that submesoscales exhibit a strong seasonal cycle (Callies et al., 2015; Rocha et al., 2016; Berta et al., 2020). Furthermore, the modulation of tracer export on seasonal time scales has recently been demonstrated (Cao & Jing, 2022; Mahadevan et al., 2020). Therefore, the primary objective of our study is to assess the seasonal impact of submesoscale processes on the vertical transport of a passive tracer released in the surface mixed layer (ML). We use a primitive-equation model in a regional configuration that allows submesoscales. We specifically focus on the North Atlantic subpolar gyre, a region known for significant seasonal variations. Moreover, this region is associated with intense phytoplankton blooms in spring when submesoscale activity is intense (Treguier et al., 2005) and is one of the most critical areas for carbon sequestration, with an average uptake

118 of about 0.55-1.94 petagrams of carbon per year, representing $\sim 12\%$ of the global net
 119 ocean uptake (Takahashi et al., 2002; Sanders et al., 2014).

120 The outline of this paper is as follows. Section 2 presents our numerical simulation.
 121 Section 3 outlines the methodology used to identify surface submesoscale fronts. Section
 122 4 describes the seasonal evolution of a tracer released within the ML and analyzes the
 123 contribution of fronts to tracer subduction. Finally, section 5 provides a detailed discus-
 124 sion of the results.

125 2 Methodology

126 2.1 Numerical setup

127 We set up a realistic simulation of the circulation in a northeastern part of the North
 128 Atlantic subpolar gyre, using the oceanic modeling system CROCO (Coastal and Re-
 129 gional Ocean COmmunity model), which resolves the primitive equations (Shchepetkin
 130 & McWilliams, 2005). A nesting approach is used here with a parent simulation (GI-
 131 GALT3) covering most of the Atlantic Ocean with a horizontal resolution of 3 km (Gula,
 132 Theetten, et al., 2021). GIGALT3 provides the nested simulation with the initial state
 133 and the lateral boundary conditions. The study domain is shown in Figure 1. It covers
 134 an area of 800 km \times 640 km, ranging from 53.8°N to 62.5°N and from 20.5°W to 37.8°W.
 135 The horizontal grid spacing $\Delta x = 800$ m is almost constant across the domain. Ver-
 136 tally, we discretize the model with 200 sigma levels, which roughly corresponds to cell
 137 heights of $\Delta z = 2$ m within the surface layer. This vertical resolution is chosen to ac-
 138 curately represent the surface dynamics. The ocean is forced at the surface by hourly
 139 atmospheric forcings from the Climate Forecast System Reanalysis using a bulk formu-
 140 lation with relative winds (Saha et al., 2010). Tidal forcing is not included. The grid bathymetry
 141 is from the global SRTM30plus dataset (Becker et al., 2009). We use the rotated-and-
 142 split 3-rd order upstream biased advection scheme (RSUP3) for temperature and salin-
 143 ity, which limits spurious diapycnal mixing and improves the representation of dynam-
 144 ical gradients (Lemarié et al., 2012). For the passive tracer, we use the 5-th order weighted
 145 and essentially non-oscillatory scheme (WENO5), to better preserves the positivity of
 146 the concentration.

147 The simulation is run for 13 months, from December 1, 2007, to December 31, 2008,
 148 with a time step of 90 seconds and produces 3-hourly averaged outputs. The first month
 149 is dedicated to the spin-up phase, ensuring that submesoscale structures have time to
 150 develop. We therefore analyse the outputs for the year 2008. To discard potential bound-
 151 ary effects, all the results are computed within a subdomain excluding points within 100
 152 km of the boundaries.

153 2.2 Tracer initialisation and equation

154 On the first day of each month, a passive tracer is released throughout the entire
 155 domain within the upper mixed layer and remains for a period of 29 days. This exper-
 156 imental design allows us to evaluate and compare both mixed-layer water subduction and
 157 deep export independently for each month. The tracer concentration C is distributed
 158 following a hyperbolic tangent profile:

$$C(x, y, z, t = 0) = \frac{1}{2} \left(1 + \tanh \left(\frac{z - z_{target}(x, y)}{dz(x, y)} \right) \right), \quad (1)$$

159 where x, y, z are the spatial coordinates, and t is time. We choose $z_{target}(x, y) =$
 160 $0.6z_{mld}(x, y)$, with z_{mld} the mixed layer depth (MLD), determined by a density differ-
 161 ence threshold of 0.03 kg m^{-3} from the surface (de Boyer Montégut et al., 2004). The
 162 distribution ensures that there is no tracer below the MLD. In addition, $dz(x, y) = \frac{1}{8}|z_{mld}(x, y)|$

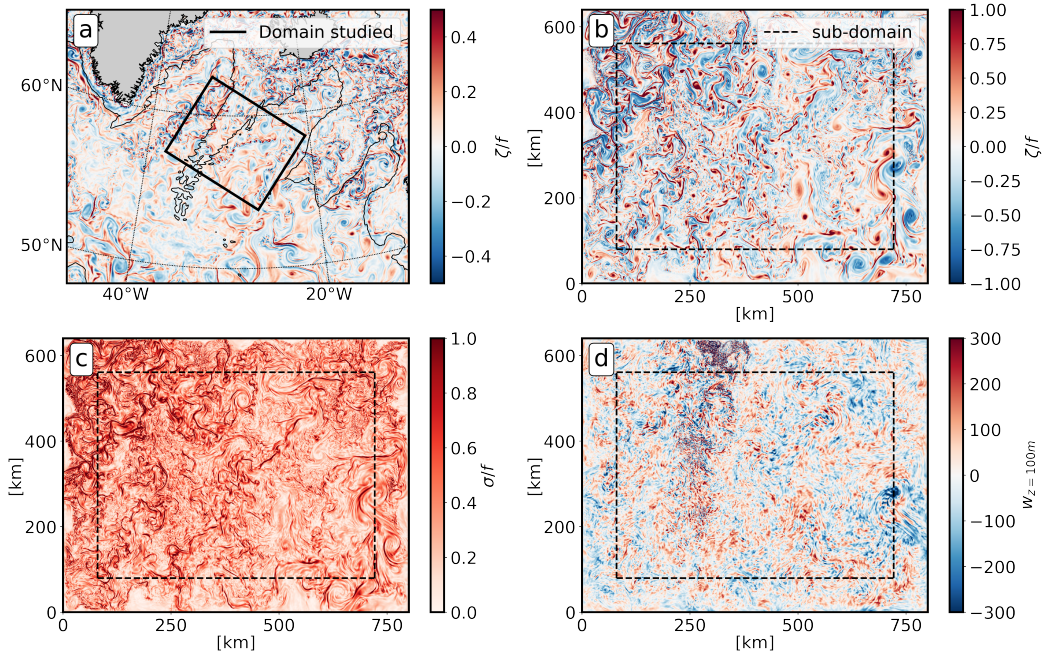


Figure 1. (a) Snapshot of the GIGATL3 simulation ($dx = 3\text{km}$) on the 8th of February . The background is the relative vorticity and the black contour is the bathymetry at 2000 m. The black rectangle is the domain of the regional simulation. (b), (c) and (d) represent the relative vorticity, the strain and vertical velocities at 100 m depth, respectively, computed from the regional simulation ($dx = 800\text{m}$). The relative vorticity and strain are normalised to the local Coriolis frequency. All the statistical results are computed in the dashed rectangle subdomain to discard boundary effects.

163 is chosen to achieve a smooth transition near the MLD to avoid numerical instability due
 164 to sharp vertical gradients in tracer concentration. Figure 2 shows an example of the tracer
 165 concentration for 3 selected days in February. It illustrates how the tracer is stirred by
 166 the mesoscale and submesoscale circulation and how it accumulates into or is depleted
 167 from frontal regions.

168 The CROCO model uses the following tracer equation:

$$\frac{\partial C}{\partial t} = -u_j \frac{\partial C}{\partial x_j} - w \frac{\partial C}{\partial z} + \kappa_c + D_c + S_c, \quad (2)$$

169 where C is the tracer concentration, u_j are the horizontal velocities, w is the vertical
 170 velocity, κ_c is the vertical diffusion, D_c is the horizontal diffusion and S_c is a source
 171 or sink term (set to zero in this study). D_c is not explicit in CROCO, but results from
 172 the implicit contribution of the upstream-biased advection scheme. Vertical mixing ($\kappa_c =$
 173 $\frac{\partial}{\partial z}(K_c \frac{\partial C}{\partial z})$) computed with the tracer diffusivity K_c is parameterized with the K-profile
 174 parametrization scheme (KPP, Large et al., 1994).

175 3 Seasonality of submesoscale fronts

176 The numerical simulation provides compelling evidence for tracer subduction driven
 177 by fronts. Figure 3 presents a vertical section of the domain on 4th April, 4 days after
 178 the tracer release. The vertical section highlights distinct fronts usually characterized

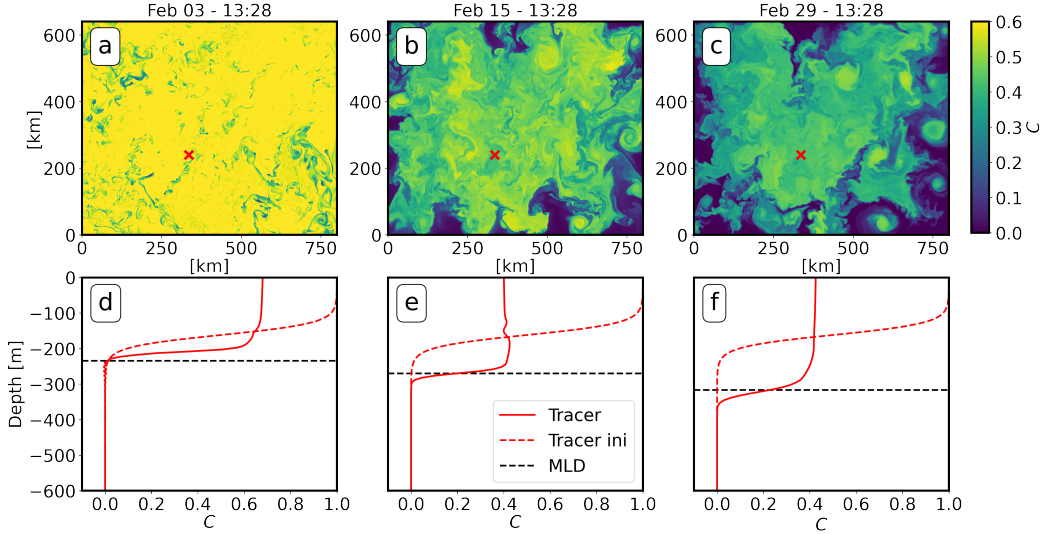


Figure 2. (a), (b) and (c) show the tracer concentration at the surface for February 3, 15 and 29. (d), (e) and (f) show the corresponding tracer vertical distribution (red line) at the location of the red cross. The dashed red line shows the initial vertical distribution of the tracer and the dashed black line is the MLD.

by significant vertical velocities ($w > 100 \text{ m day}^{-1}$) and a pronounced subduction of the tracer below the mixed layer. In this section, we first explain how we identify submesoscale fronts based on a strain and vorticity criterion and we present a first analysis to quantify the seasonal variations in the prevalence of fronts and their associated velocity field.

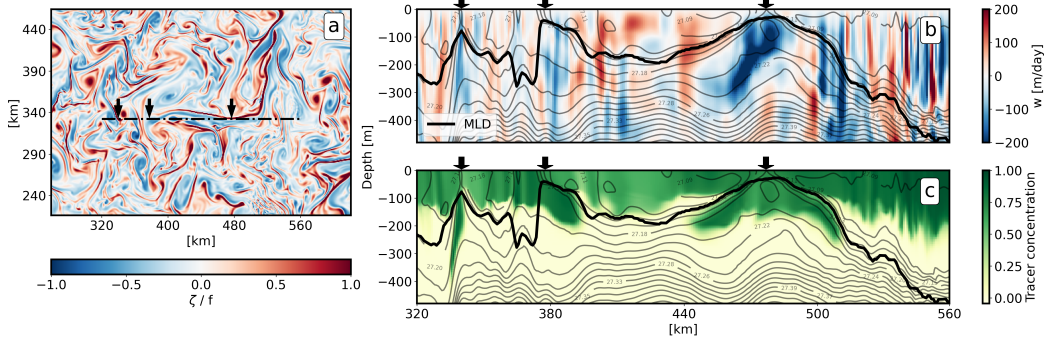


Figure 3. (a) Snapshot of the surface relative vorticity on the 4th of April. The vertical section over a front is marked with a dashed black line. The section meets several fronts denoted by the black arrows. (b) Vertical cross section. The colors represent the vertical velocities. The black line is the MLD computed with a density threshold of 0.03 kg m^{-3} from the surface. The grey lines are the isopycnals. c) Tracer concentration on the same vertical section.

184 **3.1 Seasonal variability of submesoscale fronts**

185 The dynamics of the horizontal flow can be expressed in terms of the strain ten-
 186 sor. This strain tensor can be decomposed into the vertical vorticity ζ , the horizontal
 187 divergence δ and the strain rate σ (referred to as strain in the following for simplicity)
 188 as follows:

$$\zeta = \frac{\partial v}{\partial x} - \frac{\partial u}{\partial y} ; \quad \delta = \frac{\partial u}{\partial x} + \frac{\partial v}{\partial y} ; \quad \sigma = \sqrt{\left(\frac{\partial u}{\partial x} - \frac{\partial v}{\partial y}\right)^2 + \left(\frac{\partial u}{\partial y} + \frac{\partial v}{\partial x}\right)^2} \quad (3)$$

189 Strain and vorticity are often used to identify structures such as submesoscale fronts
 190 and eddies. Figure 1 displays the vorticity and strain within the domain on 8th Febru-
 191 ary. During this winter period, we observe widespread and intense submesoscale struc-
 192 tures, which are characterized by high vorticity and strain. This signature distinguishes
 193 them from eddy structures, which typically exhibit significant vorticity but weak strain
 194 patterns (Gula et al., 2014). Therefore, a flow decomposition based on joint probabil-
 195 ity density functions of surface vorticity and strain proves valuable for identifying fronts
 196 and eddies (Shcherbina et al., 2013). Previous studies have localized submesoscale fronts
 197 in vorticity-strain space as the regions near the lines $\sigma = |\zeta|$ (Shcherbina et al., 2013;
 198 McWilliams, 2016; Balwada et al., 2021). In a strongly ageostrophic regime ($|\delta| \sim |\zeta|$;
 199 Gula et al. (2014)), Barkan et al. (2019) demonstrated that fronts tend to cluster around
 200 the lines $\sigma = \sqrt{2}|\zeta|$. However, to our knowledge, none of the previous studies have pre-
 201 cisely defined the area corresponding to submesoscale fronts. We have therefore chosen
 202 to define the frontal region by $\sigma > |\zeta|$ and with a restrictive criterion of $|\zeta/f| \sim Ro >$
 203 0.5. The Ro criterion is based on the work of Siegelman (2020), who observed in a fine
 204 resolution model that submesoscale structures above the permanent thermocline char-
 205 acterised by ageostrophic flow are associated with $Ro > 0.5$. We define two subdomains,
 206 labelled (1A) and (1C) and delineated by dots and hatches, respectively, corresponding
 207 to the anticyclonic and cyclonic submesoscale fronts (Figure 4). The separation of cy-
 208 clonic and anticyclonic fronts is useful because cyclonic fronts (1C) are known to con-
 209 tribute significantly to intense downward velocities, while anticyclonic fronts generally
 210 induce upwelling and weaker velocities (Gula, Taylor, et al., 2021). In addition, we name
 211 the two other zones dominated by vorticity based on Balwada et al. (2021): the cyclonic
 212 zone (2) defined by $\zeta/f > 0$ and $\sigma < |\zeta|$, and the anticyclonic zone, defined by $\zeta/f <$
 213 0 and $\sigma < |\zeta|$. These regions correspond to areas within anticyclonic and cyclonic ed-
 214 dies.

215 Figure 4a displays the integrated surface strain-vorticity JPDF computed over March.
 216 These statistics are computed within bins of size of 0.05×0.025 (vorticity \times strain). The
 217 contour line delineates the region containing 99.99% of the grid points. A large fraction
 218 of the surface points exhibit weak vorticity and strain ($\zeta/f < 0.5$ and $\sigma/f < 0.5$), con-
 219 sistent with the quasi-geostrophic regime of turbulence expected to develop at this model
 220 resolution. The observed asymmetry, characterised by a peak in 1C, is the signature of
 221 submesoscale fronts (McWilliams, 2016; Buckingham et al., 2016). The 99.99% contour
 222 of the surface vorticity-strain JPDF is shown for each month in Figure 4b). Each sea-
 223 son has a distinct JPDF signature, reflecting a clear shape evolution driven by the pres-
 224 ence of submesoscale dynamics. The winter period exhibits the largest domain with the
 225 highest asymmetry due to more energetic submesoscales (Callies et al., 2015), while the
 226 JPDF envelope during the summer months is confined to a region of low strain and vor-
 227 ticity. Interestingly, the peak remains significant in spring, making this period partic-
 228 ularly relevant for organic carbon export as the region hosts significant phytoplankton
 229 blooms in the euphotic layer. To quantitatively assess the presence of fronts, we calcu-
 230 late the fraction of points within regions (1A) + (1C) for each month, which we consider
 231 to be the fraction of the surface covered by fronts, hereafter simplified as the "fraction
 232 of fronts" (Red bars in Figure 5a). The frontal area is maximum in March, accounting

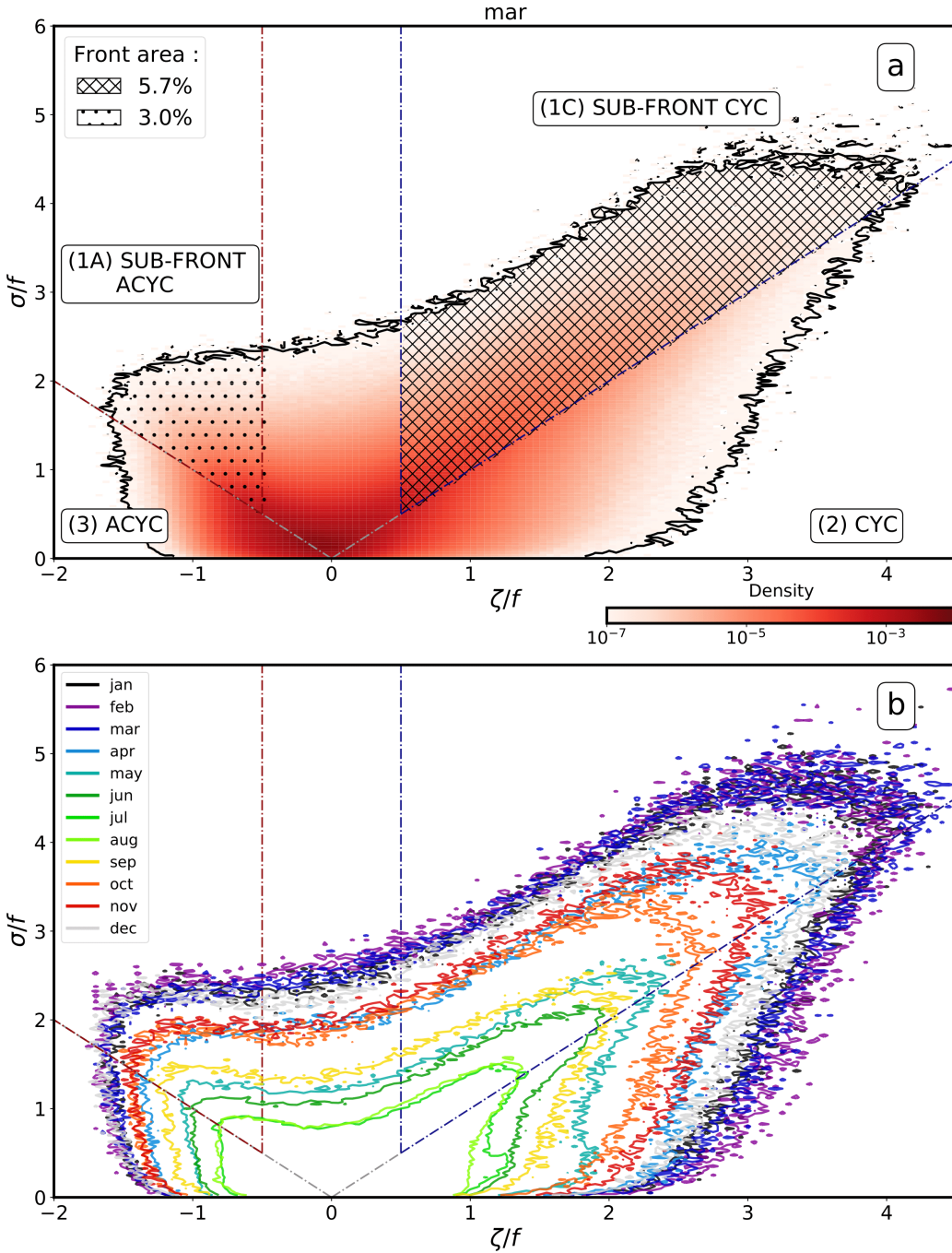


Figure 4. (a) Surface strain - vorticity JPDF in March. The black contour is the integrated domain containing 99.99% of the points. (1A) is the anticyclonic submesoscale frontal zone and (1C) is the cyclonic submesoscale frontal zone. (2) and (3) are the cyclonic and anticyclonic zones, respectively. The fraction of points within (1A) (dotted area) and (1C) (hatched area) are given. (b) Surface strain - vorticity JPDF domain contours (99.99% of the points) for each month.

for about 9% of the total area (5.7 % in 1C). Conversely, the lowest fraction of submesoscales is found in July with less than 0.5%.

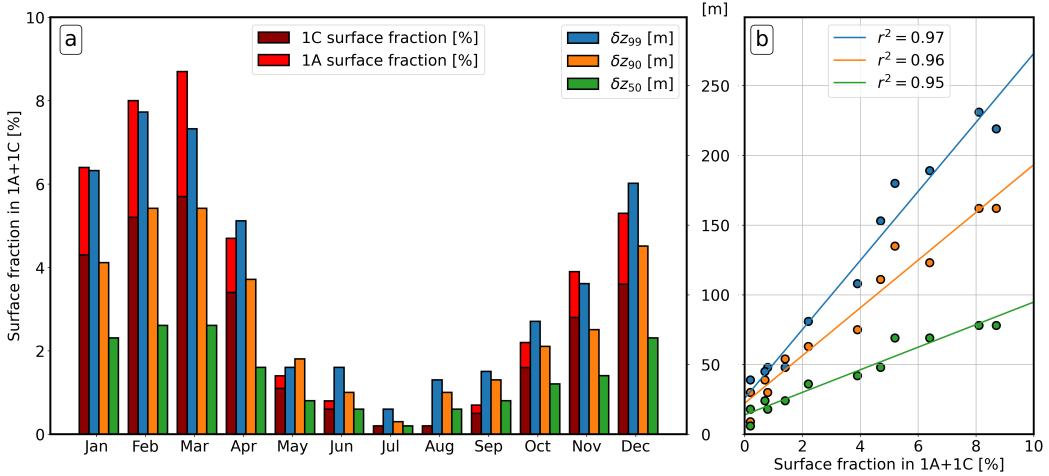


Figure 5. For section 3 : Red bars represents the surface fraction of the cyclonic (1C) and anticyclonic (1A) front area for each month (i.e sum of the the values inside the dotted and hatched area in Figure 4). For section 4 : (a) Deepening of the 50th (green δ_{50}), 90th (orange δ_{90}) and 99th (blue δ_{99}) tracer percentiles between the first and last day (29th day) for each monthly experiment. The tracer percentile z_x represents the depth above which $x\%$ of the tracer is located. (b) Linear regression between the total surface fraction of fronts in (1A) and (1C) and tracer deepening computed with the 12 monthly experiments.

235

3.2 Seasonal variability of vertical velocity

236
237
238
239
240
241
242
243
244
245
246
247

Following the approach in Balwada et al. (2021), we look at the distribution of variables at depth as a function of surface vorticity and strain. This approach reveals interesting patterns in the vertical velocity w . For each month, we computed the distribution of the bin-averaged vertical velocity \bar{w}_z (the $\bar{}$ represents the average in a bin), conditioned on surface vorticity and strain over 20 vertical z levels equally spaced from the surface to $2z_{mld}$ (z_{mld} representing the MLD). An example for March with 5 depths levels is shown in Figure 6. Similar to the JPDF, we use 3-hourly outputs (averages) during the first 29 days of each month. Our approach is similar to that of Balwada et al. (2021), with a key difference being that instead of considering a horizontally constant MLD, we compute z_{mld} at each grid point and for each time step. To analyse subduction at z_{mld} , a focus on the mean vertical velocity \bar{w}_{mld} for each month is given in Figure 7.

248
249
250
251
252
253
254
255
256
257
258
259
260
261

Although there is a monthly variability in the distribution of \bar{w}_{mld} , we observe consistent patterns. Notably, both anticyclonic (3) and cyclonic (2) features are associated with upward vertical velocities ($\bar{w}_{mld} > 0$) while the largest negative velocities are within the (1C) area. However, some observations change with depth (Figure 6). \bar{w}_z seems to be significantly weaker below z_{mld} . Focusing on the (1A) area, we also observe that \bar{w}_z changes sign with depth ($\bar{w}_z > 0$ for $z = 0.1z_{mld}$ and $\bar{w}_z < 0$ for $z < z_{mld}$). This shift may be a direct consequence of the methodological limitation. Indeed, the dynamics conditioned at depth, especially below z_{mld} , may not always be directly linked to surface properties. First, the fronts are often surface intensified and the associated secondary circulation may not extend to z_{mld} and below. In addition, vertical velocities induced by a front often follow isopycnal paths that are not vertical and include a horizontal component (Freilich & Mahadevan, 2021). Consequently, the associated subduction may not necessarily be located directly beneath its apparent surface signature, and lateral advection transport may also be induced. This is particularly problematic for the light anti-

262 cyclonic side of fronts, whose upward path may be above the dense cyclonic downward
 263 path (supplementary information Figure S1). Consequently, below a certain depth, we
 264 associate part of the cyclonic downward velocity with the (1A) area, biasing the results,
 265 especially for months associated with deep MLDs such as March. However, with the ex-
 266 ception of the (1A) area, we observe robust w patterns constrained by surface dynam-
 267 ical features, independent of season and depth. These observations support our hypoth-
 268 esis that the surface dynamics are strongly linked to the vertical velocity at the mixed
 269 layer base.

270 Focusing on the frontal areas (1A) and (1C), we compare the vertical profiles of
 271 vertical velocity for each month between $z = 0$ and $z = 2z_{mld}$. We compute the mean
 272 vertical velocity inside (1A) and (1C), $\langle w_z \rangle^{1A}$ and $\langle w_z \rangle^{1C}$ (Figure 8a,b). The maximum
 273 velocities within the fronts are typically observed at depths corresponding to $z = 0.3 -$
 274 $0.4z_{mld}$, and usually drop to a much weaker value near z_{mld} . Region (1C) is consistently
 275 associated with downward velocities, with varying seasonal intensities ranging from -130
 276 m/day (winter) to -10 m/day (summer). In contrast, region (1A) shows upward veloci-
 277 ties with values ranging from 5 m/day to 70 m/day. Below the mixed layer, $\langle w_z \rangle^{1C}$ re-
 278 mains consistently negative. However, $\langle w_z \rangle^{1A}$ switches from positive to negative values
 279 from October to March below the mixed layer, which are months associated with large
 280 MLDs. Hence, we suggest that this switch is an anomaly, possibly due to the method-
 281 ological bias mentioned above.

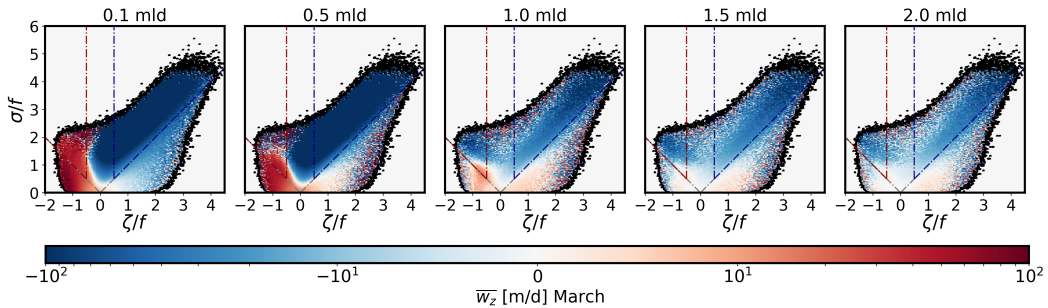


Figure 6. Bin-averaged vertical velocity conditionned on surface vorticity and strain at different vertical levels during March. The black contour is the integrated domain containing 99.99% of the points. The remaining 0.01% of points are hidden.

282 The mean vertical velocity also appears to follow a seasonal pattern. The relation-
 283 ship between the fraction of fronts and $\langle w_{mld} \rangle$ in (1A) and (1C) computed with the 12
 284 monthly experiments is shown in Figure 8c,d. It shows a moderate correlation with cor-
 285 relation coefficients $r^2 = 0.385$ in (1C) and $r^2 = 0.515$ in (1A) (Taylor, 1990; Ratner,
 286 2009). This supports the idea that vertical velocities at z_{mld} are intensified when the frac-
 287 tion of surface fronts is larger.

288 4 The seasonal tracer evolution

289 In this section we analyse the tracer transport at depth, focusing in particular on
 290 the vertical advective subduction that occurs within fronts.

291 4.1 Tracer deepening

292 We examine the tracer evolution over the vertical in Figure 9, which displays the
 293 average tracer concentration within 3-meter bins and the spatially averaged evolution
 294 of the mixed layer depth $\langle z_{mld} \rangle$. Over the study period, the mixed layer has a typical

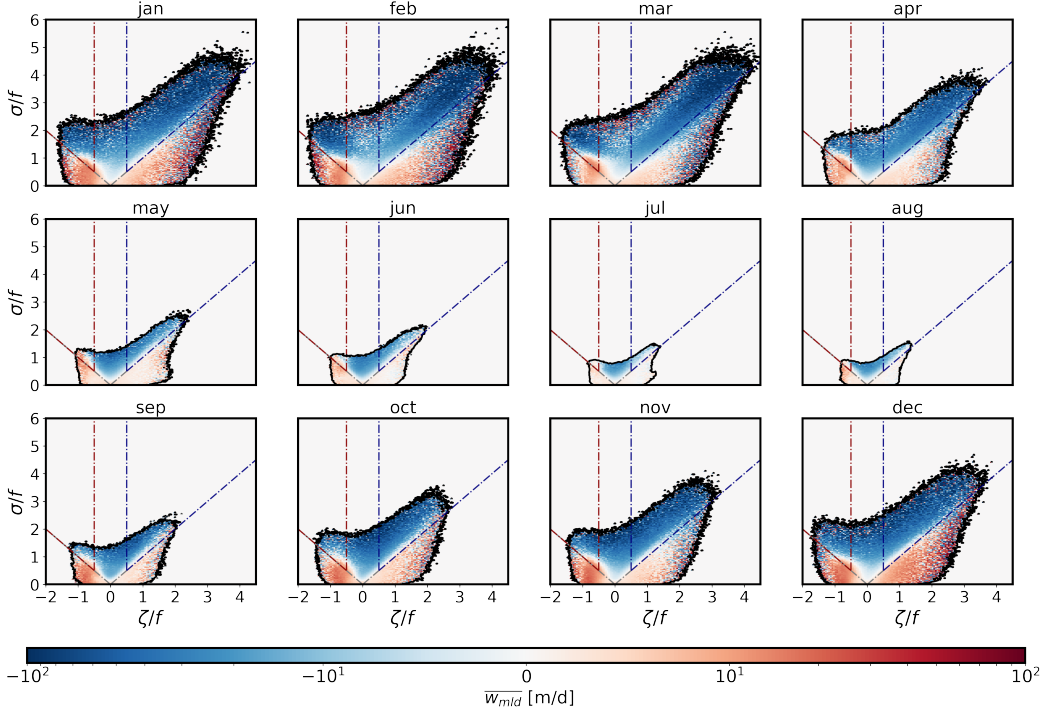


Figure 7. Bin-averaged vertical velocity at the MLD conditionned on surface vorticity and strain for each month. Black contour is the integrated domain that contain 99.99% of points (points outside have been removed).

seasonal evolution characterised by a stable and large depth in winter, intense stratification in spring, a shallow and stable depth in summer and a gradual deepening in fall. To better estimate the evolution of the tracer, we compute the distribution of the tracer concentration as a function of depth and monitor the distribution's median, 90th, and 99th percentiles. Each month the tracer spreads deeper into the water column, and its concentration within the mixed layer decreases. Note that the tracer can escape through the open boundaries of the domain, but this does not affect the statistical results. The tracer depth is particularly important for carbon export, as the carbon sequestration time is directly dependent on the depth of injection (Bol et al., 2018). The difference between the depth of each percentile on the first day and on the last day ($\delta z_{99}, \delta z_{90}, \delta z_{50}$) is plotted in Figure 5a. The varying seasonal conditions allowed us to compute the linear regression between the fraction of fronts and the tracer deepening. Interestingly, $\delta z_{99}, \delta z_{90}$ and δz_{50} appear to be significantly correlated with the front spatial footprint (Figure 5b). This indicates that the fraction of fronts impacts the depth at which the tracer is subducted. Consequently, the surface conditions can potentially be used as an indicator to estimate the redistribution of tracer at depth in this region.

4.2 Seasonal tracer subduction driven by submesoscale fronts

We mapped the vertical transport of the tracer, wC , in surface strain-vorticity space. We then summed the vertical transport within each bin, and further summed within each dynamical area to estimate their respective contribution. These quantities are computed for 20 vertical levels between the surface and $2z_{mld}$. An example for March is given in Figure 10. Inside the mixed layer, the direction of vertical transport is similar to what we observe with the mean velocity (Figure 6). This is because the tracer is almost uni-

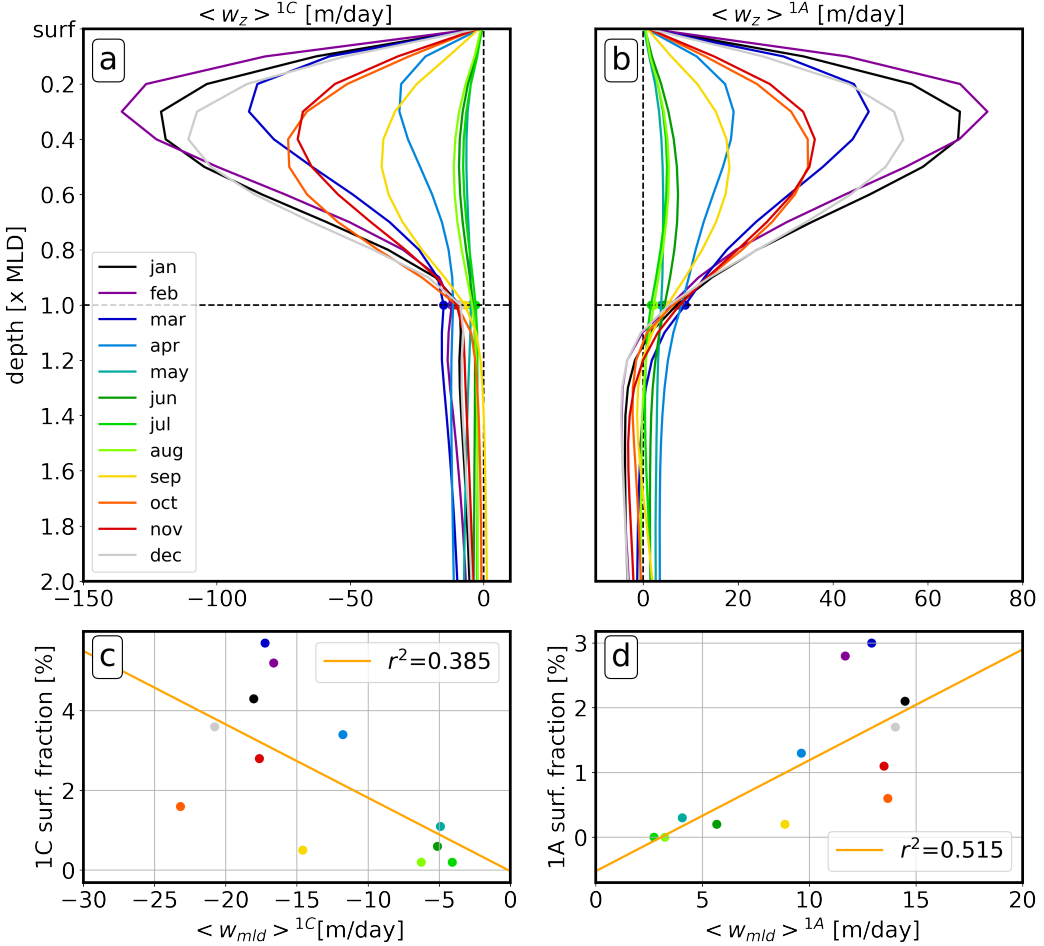


Figure 8. (a-b) Mean vertical velocity computed from grid points inside the front cyclonic area ($1C$) $\langle w_z \rangle^{1C}$ and $1A$ $\langle w_z \rangle^{1A}$. The values are computed between the surface and $z = 2z_{mld}$ for each month. (c-d) Linear regression between the mean velocity $\langle w_{mld} \rangle^{1A}, \langle w_{mld} \rangle^{1C}$ and the corresponding fraction of fronts in $1A$ and $1C$.

form across the mixed layer and always positive. Therefore, the total transport direction is directly related to the mean velocity. Below z_{mld} , however, the transport is mostly negative in each region. This is because no tracer was initially injected at this depth. A small part in the eddy region still shows positive transport, suggesting that some of the subducted tracer may be reinjected into the mixed layer. The blue contours indicate the region contributing to 50% and 99% of the downward transport. It is clear that most of the downward contribution is associated with low strain and vorticity, which is the region that largely dominates the surface dynamics (Figure 4). However, the ($1C$) area also appears to be a region that contributes significantly to the export.

Focusing on subduction, we also plotted $\Sigma w C_{mld}$ conditioned on vorticity and strain for each month in Figure 11. Irrespective of the season, the anticyclonic (3) and cyclonic (2) areas contribute mainly to the upward transport, while the remaining region is primarily associated with downward transport. Again, we observe the important contribution of the ($1C$) area, which is mainly involved in the downward fluxes.

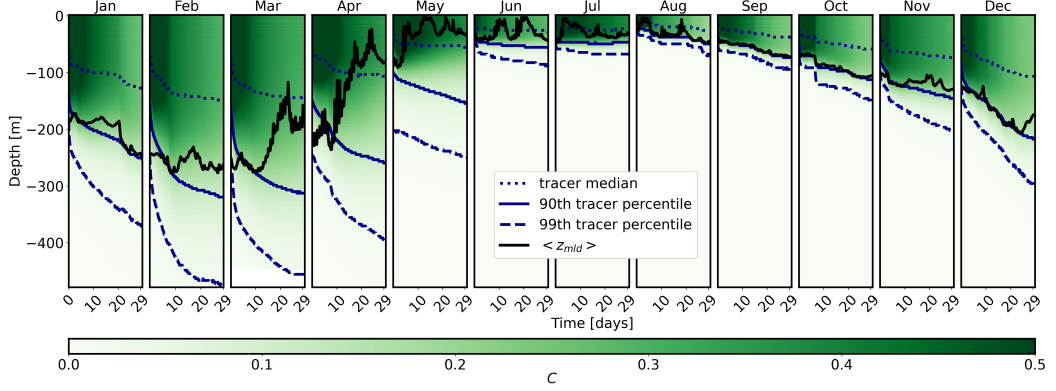


Figure 9. Tracer distribution and evolution for each month. The tracer concentration is vertically averaged over 3-meter bins. The black line is the spatial mean of the mixed layer depth computed for each time step (3h) with a density threshold. Blue lines represent the 50th (dotted), 90th (solid) and 99th (dashed) percentiles of the tracer.

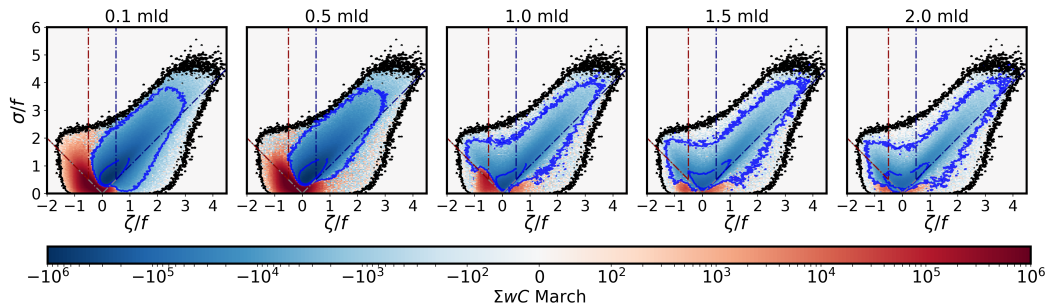


Figure 10. Sum of vertical transport ΣwC conditioned on surface vorticity and strain at different vertical levels in March. Black contour is the integrated domain containing 99.99% of the points. Points outside have been removed. Blue contours include the integrated points contributing to 50% (inside) and 99% (outside) of the total downward transport.

To confirm this trend, we calculated the total tracer fluxes for the grid points inside (1A) and (1C), $\Sigma^{1A}wC_z$ and $\Sigma^{1C}wC_z$ (Figures 12a and 12b). We also estimated the fraction of these fluxes relative to the total downward advective fluxes F_z^{1A} and F_z^{1C} at depth z such as $F_z^{1C} = \frac{\Sigma^{1C}wC_z}{\Sigma^{wC_z < 0}wC_z}$ and $F_z^{1A} = \frac{\Sigma^{1A}wC_z}{\Sigma^{wC_z < 0}wC_z}$ (Figures 12c and d). Similar to w , the transport wC in (1C) and (1A) reaches a peak at $0.3 - 0.4z_{mld}$ and decreases significantly near z_{mld} . In (1C), the transport remains always negative and can contribute significantly to the total downward transport between the surface and $2z_{mld}$. In (1A), however, the transport shifts from positive to negative precisely at z_{mld} . As mentioned in section 3.2, the result below z_{mld} in the (1A) region may be affected by a methodological bias, making any interpretation difficult.

We observe a singularity at z_{mld} in Figures 12c,d. This is due to the total downward fluxes $\Sigma^{wC_{mld} < 0}wC_{mld}$ (not shown), which have a local extremum at this depth. At present, this maximum is not fully understood, but it is likely to be related to the MLD singularity itself. We therefore focus on the two depths $0.9z_{mld}$ and $1.1z_{mld}$ to obtain a more robust description. As mentioned above, in (1A) we observe a shift in the sign of ΣwC , from positive (i.e. obduction) to negative (i.e. subduction). Overall, the net fluxes near z_{mld} are close to 0, indicating that (1A) does not contribute significantly to

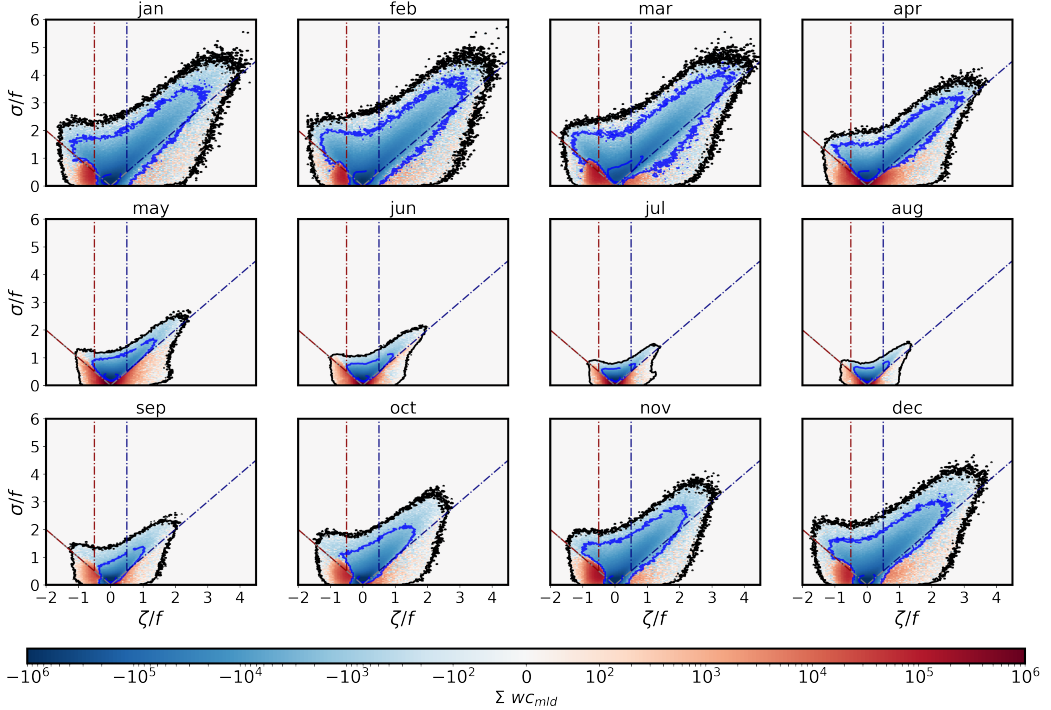


Figure 11. The sum of vertical advection $\Sigma w_{mid} \cdot C_{mid}$ conditioned by surface vorticity and strain. Integrated blue contours indicate 99% and 50% of the total negative flux $\Sigma^{wc_z < 0} wc_z$. The black contour contains 99.99% of the points (points outside have been hidden).

subduction, the absolute contribution being $F_{mld}^{1A} = 1\text{--}5\%$. Conversely, the fluxes associated with (1C) at z_{mld} are important and represent a significant contribution in terms of subduction, particularly during the winter and spring months, with a contribution of $F_{mld}^{1C} = 30\text{--}40\%$ of the total downward flux. There is a slight decrease in the contribution with depth, which again could be due to the limitation of the methodology. Considering the 12 monthly experiments, we find the evidence of a clear relationship between the tracer fluxes, the subduction contribution terms around z_{mld} , and the fraction of fronts (Figures 12e-h). In particular, $\Sigma^{1C} wC_z$ and F_{mld}^{1C} show a direct correlation with the fraction of fronts ($r^2 = 0.90\text{--}0.92$). The linear relationship is also observed for the anticyclonic front, but not as effective ($r^2 = 0.66\text{--}0.74$). This results suggests that, in this region, the frontal vertical advective subduction contribution can be estimated from the surface strain-vorticity.

5 Discussion

5.1 Bias and future improvements

Few studies have used surface strain-vorticity statistical tools to characterise submesoscale dynamics in both observations and models (Shcherbina et al., 2013; Rocha et al., 2016; Balwada et al., 2021; Vic et al., 2022; Wang et al., 2022; Cao et al., 2023). To our knowledge, Balwada et al. (2021); Cao et al. (2023) are the only studies that uses JPDFs and vertical tracer transport conditioned on surface strain and vorticity to estimate the submesoscale frontal contribution at depth.

Results from numerical simulations can be highly sensitive to the grid resolution (supporting information Figure S2). By increasing the resolution grid from 3 km to 0.8

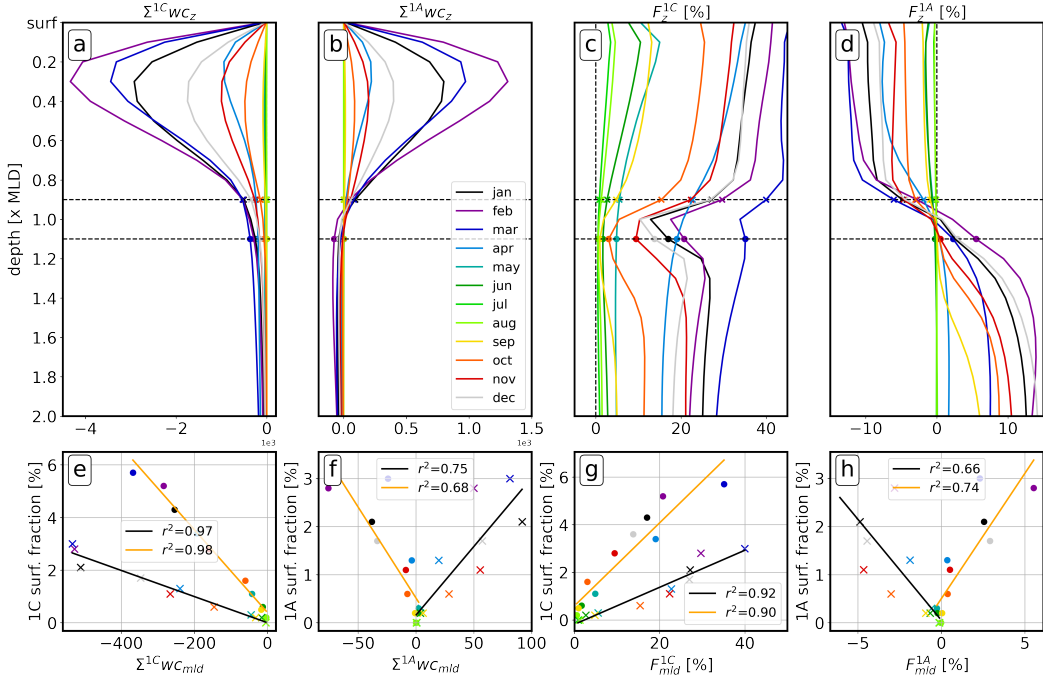


Figure 12. (a-b) Sum of the tracer fluxes in (1C) and (1A) between surface and $2.z_{mld}$. (c-d) Fraction tracer fluxes computed in (1A) and (1C) relative to the total advective downward fluxes. (e-f) Corresponding linear regressions between the fraction of fronts and tracer fluxes in (1A) and (1C) at z_{mld} . (g-h) Linear regressions between the fraction of fronts and the corresponding fraction of fluxes relative to the total advective downward fluxes $\Sigma^{wc_{mld}<0}wc_{mld}$. The linear regressions are computed with the 12 monthly experiments.

km, we find that the front fraction increases significantly from 0.2% to 3.8%, and so far it is challenging to quantify the part of the submesoscale not resolved here. One of the main sources of submesoscale fronts is the mixed-layer baroclinic instability (MLI), whose scale $lsml$ has been estimated by Dong et al. (2020) (supporting information Figure S3). With a 0.8 km grid resolution, the effective resolution ($4\Delta x = 3.2$ km) should be sufficient to resolve MLI in the region in winter ($lsml \sim 12$ km). However, the scale of MLI in summer is lower ($lsml \sim 3$ km) and it is possible that MLI is not fully resolved here, which could explain why the front contribution found during this period is very weak. However, the scale at which the fronts are arrested is smaller than the MLI scale (Bodner et al., 2023), especially in winter where it is well below the effective resolution of the model, but it may be marginally resolved in summer. Other submesoscale instabilities, such as symmetric instabilities (Bachman et al., 2017), are unresolved throughout the year (Dong et al., 2021). And we can only speculate that their inclusion could lead to additional mixing at the base of the mixed layer and increased exchange between mixed layer and thermocline water in some regimes. We do not expect internal gravity waves (IGW) to play a direct first-order role in vertical tracer fluxes, as shown in Balwada et al. (2018) and Balwada et al. (2021), but we might expect IGW to play a role in generating additional vertical mixing at the base of the mixed layer and in tracer fluxes through the ML base, especially for near-inertial internal waves (NIW) (Alford, 2020) and even some higher-frequency IGW (Barton et al., 2001; Wain et al., 2015).

The implicit mixing associated with the advection of the passive tracer may also play a role at the base of the mixed layer, where the parameterized vertical mixing de-

393 creases to its background value, and will need to be quantified more precisely. Since we
 394 expect subduction to occur along isopycnals beneath the mixed layer, even small diapycnal
 395 effects could affect tracer dispersion. The RSUP3 scheme used for the advection of
 396 potential temperature and salinity minimizes such effects, but the WENO5 scheme used
 397 for the passive tracer – to better preserve the positivity of its concentration – has the
 398 disadvantage of leading to slightly higher diapycnal diffusivities.

399 Also, due to numerical storage limitations, we chose to use 3-h averaged outputs
 400 here. This output frequency slightly smooths the frontal influence compared to hourly
 401 snapshots, resulting in a 0.5% loss in frontal fraction (Supporting Information Figure S4).
 402 For all these reasons, our results may underestimate the influence of the front on tracer
 403 transport, especially in summer.

404 Another important limitation of our study is the connection between the surface
 405 dynamics and the dynamics at depth, as mentioned in section 3.2. In particular, the ver-
 406 tical velocities induced by a front are limited in depth and do not always follow a 1D ver-
 407 tical direction. Furthermore, the vertical structure of the fronts can be more complex
 408 and is not always surface intensified, as discussed in Wang et al. (2022). These limita-
 409 tions result in a bias that may be depth dependent and needs to be properly quantified
 410 in order to better understand the limited zone where such a method can be applied. This
 411 implies that the frontal isopycnal paths need to be accurately determined, which is a chal-
 412 lenging task that remains to be addressed.

413 Finally, the definitions of the submesoscale frontal regions (1A) and (1C) used here
 414 are based on simplified assumptions. While these definitions provide reasonable approx-
 415 imations for estimating the initial impact of submesoscale fronts, they require further
 416 refinement. In reality, the definition of a submesoscale frontal region is more complex
 417 and may depend on the dynamics itself. Buckingham et al. (2016) demonstrated that
 418 ζ values in submesoscale regions are influenced by the Coriolis frequency and by the ra-
 419 tio of lateral to vertical buoyancy gradients. The Ro criteria used in our study may not
 420 be fully appropriate in certain regions, such as the Gulf Stream, where Ro is about 0.7–1.0
 421 at the submesoscale, exceeding the values in our region. Therefore, we highlight the need
 422 for further theoretical development to precisely define a submesoscale zone within the
 423 surface strain-vorticity space. This will be crucial in the future for accurate estimation
 424 of tracer export influenced by submesoscale dynamics.

425 However, compared to previous studies, we observe similar associations between
 426 surface properties and transport at the MLD, and we also find similar orders of magni-
 427 tude in terms of submesoscale contributions, reinforcing our confidence in the results.

428 5.2 Towards a better parameterization of the effect of fronts on tracer 429 subduction

430 The main objective of this study was to gain a better understanding of the con-
 431 tribution of fronts to water subduction in a seasonal perspective. Proper quantification
 432 of subduction is crucial for understanding complex ocean mechanisms such as the car-
 433 bon pump and heat transfer. Our seasonal study has allowed us to clearly identify front
 434 signatures and evaluate their impact on the transport of upper layer water to depth. Sig-
 435 nificant variations in the fraction of fronts allow us to infer a parameterization of the im-
 436 pact of fronts on tracer transport based solely on their surface characteristics. An im-
 437 portant result is that the vertical advective subduction contribution can be estimated
 438 directly from the surface dynamics. So far, it is challenging to detect submesoscale fea-
 439 tures with sea surface height (Ballarotta et al., 2019). However, with the ongoing Sur-
 440 face Water and Ocean Topography (SWOT) mission (Fu & Ubelmann, 2014; Fu et al.,
 441 2024), it will soon be possible to improve the altimetry resolution to 10–30 km. This will
 442 allow better determination of the fraction of fronts and associated subduction rates, which
 443 is particularly relevant for biogeochemical studies focusing on the contribution of sub-

mesoscale features to the biological carbon pump, often referred to as the eddy-subduction pump (Boyd et al., 2019). Despite numerous studies on the topic (Omand et al., 2015; Stukel et al., 2017), there is still no consensus quantifying at a global scale the role of submesoscale processes capable of injecting particles to depth. Yet, this may partly explain why the carbon demand of the mesopelagic ecosystem exceeds the downward flux of presumably sinking POC by a factor of 2-3 (Burd et al., 2010). While this study used a simplified approach with homogenized tracer initialization within the ML, the same methodology could be adapted to study the front's contribution to carbon export and nutrient injection using coupled biochemical modeling. In addition, it is important to note that the seasonal results presented here are based on one year of data, and interannual variability can be significant (Berta et al., 2020). Further studies are needed to assess the sensitivity associated with different time periods, regions, and numerical models. Note that our study does not address the fate of passive tracers once they leave the surface mixed layer. We expect restratification processes, driven by, e.g., springtime warming or submesoscale instabilities (Boccaletti et al., 2007), to seal the longer-term trapping of tracers below the mixed layer. These processes must be taken into account to investigate the interannual fate of tracers that leave the mixed layer.

6 Conclusion

The present study investigates the seasonal fate of a passive tracer released monthly in the surface mixed layer using a realistic high-resolution simulation in the North Atlantic. Using surface strain and vorticity criteria, we identified and quantified the fraction of surface area occupied by fronts for each month over a year. Our observations revealed a deep subduction of the tracer in the presence of submesoscale activity and a consistent correlation between front spatial footprint and tracer sinking emerged, independent of the mixed layer depth evolution. Remarkably, our investigation revealed that cyclonic submesoscale fronts, ranging from 0.5% in summer to about 6% of the surface in winter, contribute significantly to the total tracer vertical advective subduction, ranging from 0.5% to 40%, respectively. These results not only confirm the efficacy of using surface vorticity-strain criteria for front analysis, but also emphasize the need to study fronts from a seasonal perspective.

Acknowledgments

T.P. received a Ph.D. grant from École Normale Supérieure Paris-Saclay. This work was also supported by the ISblue project, an Interdisciplinary graduate school for the blue planet (ANR-17-EURE-0015), and co-funded by a grant from the French government under the program "Investissements d'Avenir". J.G. would like to acknowledge support from the French National Agency for Research (ANR) through the project DEEPER (ANR-19-CE01-0002-01). Simulations were performed using HPC resources from GENCI-TGCC (Grants 2022-A0090112051), and from HPC facilities DATARMOR of "Pôle de Calcul Intensif pour la Mer" at Ifremer Brest France. The authors thank Roy Barkan for valuable discussions.

Open Research

The codes used in this study are available online at <https://github.com/TheoPcrd/RREX2008> (Picard, 2023). The numerical simulation outputs are available on request.

References

- Alford, M. H. (2020). Revisiting near-inertial wind work: Slab models, relative stress, and mixed layer deepening. *Journal of Physical Oceanography*, 50(11),

- 3141–3156. doi: 10.1175/JPO-D-20-0105.1

Bachman, S. D., Fox-Kemper, B., Taylor, J. R., & Thomas, L. N. (2017). Parameterization of Frontal Symmetric Instabilities. I: Theory for Resolved Fronts. *Ocean Modelling*, 109, 72–95. Retrieved from <http://dx.doi.org/10.1016/j.ocemod.2016.12.003>

Ballarotta, M., Ubelmann, C., Pujol, M. I., Taburet, G., Fournier, F., Legeais, J. F., ... Picot, N. (2019). On the resolutions of ocean altimetry maps. *Ocean Science*, 15(4), 1091–1109. doi: 10.5194/os-15-1091-2019

Balwada, D., Smith, K. S., & Abernathey, R. (2018). Submesoscale Vertical Velocities Enhance Tracer Subduction in an Idealized Antarctic Circumpolar Current. *Geophysical Research Letters*, 45(18), 9790–9802. Retrieved from <https://agupubs.onlinelibrary.wiley.com/doi/10.1029/2018GL079244> doi: 10.1029/2018GL079244

Balwada, D., Xiao, Q., Smith, S., Abernathey, R., & Gray, A. R. (2021). Vertical fluxes conditioned on vorticity and strain reveal submesoscale ventilation. *Journal of Physical Oceanography*. doi: 10.1175/jpo-d-21-0016.1

Barkan, R., Molemaker, M. J., Srinivasan, K., McWilliams, J. C., & D'asaro, E. A. (2019). The role of horizontal divergence in submesoscale frontogenesis. *Journal of Physical Oceanography*, 49(6), 1593–1618. doi: 10.1175/JPO-D-18-0162.1

Barton, E. D., Inall, M. E., Sherwin, T. J., & Torres, R. (2001). Vertical structure, turbulent mixing and fluxes during Lagrangian observations of an upwelling filament system off Northwest Iberia. *Progress in Oceanography*, 51(2-4), 249–267. doi: 10.1016/S0079-6611(01)00069-6

Becker, J. J., Sandwell, D. T., Smith, W. H. F., Braud, J., Binder, B., Depner, J., ... Weatherall, P. (2009). Global Bathymetry and Elevation Data at 30 Arc Seconds Resolution: SRTM30_PLUS. *Marine Geodesy*, 32(4), 355–371. Retrieved from <https://doi.org/10.1080/01490410903297766> doi: 10.1080/01490410903297766

Berta, M., Griffa, A., Haza, A. C., Horstmann, J., Huntley, H. S., Ibrahim, R., ... Poje, A. C. (2020). Submesoscale Kinematic Properties in Summer and Winter Surface Flows in the Northern Gulf of Mexico. *Journal of Geophysical Research: Oceans*, 125(10), e2020JC016085. Retrieved from <https://agupubs.onlinelibrary.wiley.com/doi/10.1029/2020JC016085> doi: 10.1029/2020JC016085

Boccaletti, G., Ferrari, R., & Fox-Kemper, B. (2007). Mixed layer instabilities and restratification. *Journal of Physical Oceanography*, 37(9), 2228–2250. doi: 10.1175/JPO3101.1

Bodner, A. S., Fox-Kemper, B., Johnson, L., VAN ROEKEL, L. P., McWilliams, J. C., Sullivan, P. P., ... Dong, J. (2023). Modifying the Mixed Layer Eddy Parameterization to Include Frontogenesis Arrest by Boundary Layer Turbulence. *Journal of Physical Oceanography*, 53(1), 323–339. doi: 10.1175/JPO-D-21-0297.1

Bol, R., Henson, S. A., Rumyantseva, A., & Briggs, N. (2018). High-Frequency Variability of Small-Particle Carbon Export Flux in the Northeast Atlantic. *Global Biogeochemical Cycles*, 32(12), 1803–1814. doi: 10.1029/2018GB005963

Bopp, L., Resplandy, L., Orr, J. C., Doney, S. C., Dunne, J. P., Gehlen, M., ... Vichi, M. (2013). Multiple stressors of ocean ecosystems in the 21st century: Projections with CMIP5 models. *Biogeosciences*, 10(10), 6225–6245. doi: 10.5194/bg-10-6225-2013

Boyd, P. W., Claustre, H., Levy, M., Siegel, D. A., & Weber, T. (2019). Multi-faceted particle pumps drive carbon sequestration in the ocean. *Nature*, 568(7752), 327–335. doi: 10.1038/s41586-019-1098-2

Buckingham, C. E., Naveira Garabato, A. C., Thompson, A. F., Brannigan, L., Lazar, A., Marshall, D. P., ... Belcher, S. E. (2016). Seasonality of sub-

- mesoscale flows in the ocean surface boundary layer. *Geophysical Research Letters*, 43(5), 2118–2126. doi: 10.1002/2016GL068009
- Burd, A. B., Hansell, D. A., Steinberg, D. K., Anderson, T. R., Arístegui, J., Baltar, F., ... Tanaka, T. (2010). Assessing the apparent imbalance between geochemical and biochemical indicators of meso- and bathypelagic biological activity: What the @\$\$! is wrong with present calculations of carbon budgets? *Deep-Sea Research Part II: Topical Studies in Oceanography*, 57(16), 1557–1571. doi: 10.1016/j.dsr2.2010.02.022
- Callies, J., Ferrari, R., Klymak, J. M., & Gula, J. (2015). Seasonality in submesoscale turbulence. *Nature Communications*, 6(1), 6862. Retrieved from <https://doi.org/10.1038/ncomms7862> doi: 10.1038/ncomms7862
- Cao, H., Fox-Kemper, B., Jing, Z., Song, X., & Liu, Y. (2023). Towards the Upper-Ocean Unbalanced Submesoscale Motions in the Oleander Observations. *Journal of Physical Oceanography*, 53(4), 1123–1138. doi: 10.1175/JPO-D-22-0134.1
- Cao, H., & Jing, Z. (2022). Submesoscale ageostrophic motions within and below the mixed layer of the northwestern Pacific Ocean. *Journal of Geophysical Research: Oceans*. Retrieved from <https://onlinelibrary.wiley.com/doi/10.1029/2021JC017812> doi: 10.1029/2021JC017812
- Capet, X., Campos, E. J., & Paiva, A. M. (2008). Submesoscale activity over the Argentinian shelf. *Geophysical Research Letters*, 35(15), L15605. Retrieved from <http://doi.wiley.com/10.1029/2008GL034736> doi: 10.1029/2008GL034736
- Chelton, D. B., Schlax, M. G., & Samelson, R. M. (2011). Global observations of nonlinear mesoscale eddies. *Progress in Oceanography*, 91(2), 167–216. doi: 10.1016/j.pocean.2011.01.002
- de Boyer Montégut, C., Madec, G., Fischer, A. S., Lazar, A., & Iudicone, D. (2004). Mixed layer depth over the global ocean: An examination of profile data and a profile-based climatology. *Journal of Geophysical Research*, 109(C12), C12003. Retrieved from <http://doi.wiley.com/10.1029/2004JC002378> doi: 10.1029/2004JC002378
- Dong, J., Fox-Kemper, B., Zhang, H., & Dong, C. (2020). The scale of submesoscale baroclinic instability globally. *Journal of Physical Oceanography*, 50(9), 2649–2667. doi: 10.1175/JPO-D-20-0043.1
- Dong, J., Fox-Kemper, B., Zhang, H., & Dong, C. (2021). The scale and activity of symmetric instability estimated from a global submesoscale-permitting ocean model. *Journal of Physical Oceanography*, 51(5), 1655–1670. doi: 10.1175/JPO-D-20-0159.1
- Fox-Kemper, B., Adcroft, A., Böning, C. W., Chassignet, E. P., Curchitser, E., Danabasoglu, G., ... Yeager, S. G. (2019). *Challenges and prospects in ocean circulation models* (Vol. 6). Frontiers Media S.A. doi: 10.3389/fmars.2019.00065
- Freilich, M., & Mahadevan, A. (2021). Coherent Pathways for Subduction From the Surface Mixed Layer at Ocean Fronts. *Journal of Geophysical Research: Oceans*, 126(5), e2020JC017042. Retrieved from <https://onlinelibrary.wiley.com/doi/10.1029/2020JC017042> doi: 10.1029/2020JC017042
- Fu, L. L., Pavelsky, T., Cretaux, J. F., Morrow, R., Farrar, J. T., Vaze, P., ... Dibarboure, G. (2024). The Surface Water and Ocean Topography Mission: A Breakthrough in Radar Remote Sensing of the Ocean and Land Surface Water. *Geophysical Research Letters*, 51(4), 1–9. doi: 10.1029/2023GL107652
- Fu, L. L., & Ubelmann, C. (2014). On the transition from profile altimeter to swath altimeter for observing global ocean surface topography. *Journal of Atmospheric and Oceanic Technology*, 31(2), 560–568. doi: 10.1175/JTECH-D-13-00109.1
- Gula, J., Molemaker, J. J., & Mcwilliams, J. C. (2014). Submesoscale cold filaments

- in the Gulf Stream. *Journal of Physical Oceanography*, 44(10), 2617–2643. doi: 10.1175/JPO-D-14-0029.1
- Gula, J., Taylor, J., Shcherbina, A., & Mahadevan, A. (2021). Submesoscale processes and mixing. In *Ocean mixing: Drivers, mechanisms and impacts* (pp. 181–214). Elsevier. doi: 10.1016/B978-0-12-821512-8.00015-3
- Gula, J., Theetten, S., Cambon, G., & Roullet, G. (2021, June). *Description of the gigatl simulations*. Zenodo. Retrieved from <https://doi.org/10.5281/zenodo.4948523> doi: 10.5281/zenodo.4948523
- Klein, P., & Lapeyre, G. (2009). *The oceanic vertical pump induced by mesoscale and submesoscale turbulence* (Vol. 1). doi: 10.1146/annurev.marine.010908.163704
- Lacour, L., Briggs, N., Claustre, H., Ardyna, M., & Dall'Olmo, G. (2019). The Intraseasonal Dynamics of the Mixed Layer Pump in the Subpolar North Atlantic Ocean: A Biogeochemical-Argo Float Approach. *Global Biogeochemical Cycles*, 33(3), 266–281. doi: 10.1029/2018GB005997
- Lapeyre, G., & Klein, P. (2006). Impact of the small-scale elongated filaments on the oceanic vertical pump [Article]., 64(6), 835–851. doi: 10.1357/002224006779698369
- Large, W. G., McWilliams, J. C., & Doney, S. C. (1994). Oceanic vertical mixing: A review and a model with a nonlocal boundary layer parameterization. *Reviews of Geophysics*, 32(4), 363. Retrieved from <http://doi.wiley.com/10.1029/94RG01872> doi: 10.1029/94RG01872
- Lemarié, F., Debreu, L., Shchepetkin, A., & Mcwilliams, J. C. (2012). On the stability and accuracy of the harmonic and biharmonic isoneutral mixing operators in ocean models. *Ocean Modell.*, 52, 9–35. doi: 10.1016/j.ocemod.2012.04.007
- Lévy, M., Couespel, D., Haëck, C., Keerthi, M., Mangolte, I., & Prend, C. J. (2024). The Impact of Fine-Scale Currents on Biogeochemical Cycles in a Changing Ocean. *Annual Review of Marine Science*, 16(1), 1–25. doi: 10.1146/annurev-marine-020723-020531
- Lévy, M., Franks, P. J., & Smith, K. S. (2018). *The role of submesoscale currents in structuring marine ecosystems* (Vol. 9) (No. 1). Nature Publishing Group. doi: 10.1038/s41467-018-07059-3
- Llort, J., Langlais, C., Matear, R., Moreau, S., Lenton, A., & Strutton, P. G. (2018). Evaluating Southern Ocean Carbon Eddy-Pump From Biogeochemical-Argo Floats. *Journal of Geophysical Research: Oceans*, 123(2), 971–984. doi: 10.1002/2017JC012861
- Mahadevan, A. (2016). The Impact of Submesoscale Physics on Primary Productivity of Plankton. *Annual Review of Marine Science*, 8(1), 161–184. Retrieved from <https://www.annualreviews.org/doi/10.1146/annurev-marine-010814-015912> doi: 10.1146/annurev-marine-010814-015912
- Mahadevan, A., Pascual, A., Rudnick, D. L., Ruiz, S., Tintoré, J., & D'Asaro, E. (2020). Coherent pathways for vertical transport from the surface ocean to interior. *Bulletin of the American Meteorological Society*, 101(11), E1996–E2004. doi: 10.1175/BAMS-D-19-0305.1
- Mahadevan, A., & Tandon, A. (2006). An analysis of mechanisms for submesoscale vertical motion at ocean fronts. *Ocean Modelling*, 14(3-4), 241–256. doi: 10.1016/j.ocemod.2006.05.006
- McWilliams, J. C. (2016). *Submesoscale currents in the ocean* (Vol. 472) (No. 2189). Royal Society of London. doi: 10.1098/rspa.2016.0117
- McWilliams, J. C. (2021). Oceanic Frontogenesis. *Annual Review of Marine Science*, 13(1), 227–253. Retrieved from <https://www.annualreviews.org/doi/10.1146/annurev-marine-032320-120725> doi: 10.1146/annurev-marine-032320-120725
- Omand, M. M., D'Asaro, E. A., Lee, C. M., Perry, M. J., Briggs, N., Cetinić, I., & Mahadevan, A. (2015). Eddy-driven subduction exports particulate or-

- 655 ganic carbon from the spring bloom. *Science*, 348(6231), 222–225. doi:
 656 10.1126/science.1260062
- 657 Picard, T. (2023). *Code for seasonal tracer subduction in the Subpolar North At-*
 658 *lantic driven by submesoscale fronts*. Zenodo. Retrieved from <https://doi.org/10.5281/zenodo.10245485> doi: 10.5281/zenodo.10245485
- 660 Pietri, A., Capet, X., D'ovidio, F., Levy, M., Sommer, J. L., Molines, J. M., &
 661 Giordani, H. (2021). Skills and limitations of the adiabatic omega equa-
 662 tion: How effective is it to retrieve oceanic vertical circulation at mesoscale
 663 and submesoscale? *Journal of Physical Oceanography*, 51(3), 931–954. doi:
 664 10.1175/JPO-D-20-0052.1
- 665 Ratner, B. (2009). The correlation coefficient: Its values range between 1/1, or do
 666 they. *Journal of Targeting, Measurement and Analysis for Marketing*, 17(2),
 667 139–142. doi: 10.1057/jt.2009.5
- 668 Rocha, C. B., Gille, S. T., Chereskin, T. K., & Menemenlis, D. (2016). Seasonal-
 669 ity of submesoscale dynamics in the Kuroshio Extension. *Geophysical Research
 670 Letters*, 43(21), 11,304–11,311. doi: 10.1002/2016GL071349
- 671 Saha, S., Moorthi, S., Pan, H.-L., Wu, X., Wang, J., Nadiga, S., ... Goldberg, M.
 672 (2010). The NCEP Climate Forecast System Reanalysis. *Bulletin of the
 673 American Meteorological Society*, 91(8), 1015–1058. Retrieved from https://journals.ametsoc.org/view/journals/bams/91/8/2010bams3001_1.xml
 674 doi: <https://doi.org/10.1175/2010BAMS3001.1>
- 675 Sanders, R., Henson, S. A., Koski, M., De La Rocha, C. L., Painter, S. C., Poult-
 676 ton, A. J., ... Martin, A. P. (2014). The Biological Carbon Pump in
 677 the North Atlantic. *Progress in Oceanography*, 129(PB), 200–218. doi:
 678 10.1016/j.pocean.2014.05.005
- 679 Shchepetkin, A. F., & McWilliams, J. C. (2005). The regional oceanic modeling
 680 system (ROMS): A split-explicit, free-surface, topography-following-coordinate
 681 oceanic model. *Ocean Modelling*, 9(4). doi: 10.1016/j.ocemod.2004.08.002
- 682 Shcherbina, A. Y., D'Asaro, E. A., Lee, C. M., Klymak, J. M., Molemaker, M. J.,
 683 & McWilliams, J. C. (2013). Statistics of vertical vorticity, divergence, and
 684 strain in a developed submesoscale turbulence field. *Geophysical Research
 685 Letters*, 40(17), 4706–4711. Retrieved from <http://doi.wiley.com/10.1002/grl.50919> doi: 10.1002/grl.50919
- 686 Siegelman, L. (2020). Energetic submesoscale dynamics in the ocean interior. *Jour-
 687 nal of Physical Oceanography*, 50(3), 727–749. doi: 10.1175/JPO-D-19-0253.1
- 688 Siegelman, L., Klein, P., Rivière, P., Thompson, A. F., Torres, H. S., Flexas,
 689 M., & Menemenlis, D. (2020). Enhanced upward heat transport at
 690 deep submesoscale ocean fronts. *Nature Geoscience*, 13(1), 50–55. doi:
 691 10.1038/s41561-019-0489-1
- 692 Stukel, M. R., Aluwihare, L. I., Barbeau, K. A., Chekalyuk, A. M., Goericke,
 693 R., Miller, A. J., ... Landry, M. R. (2017). Mesoscale ocean fronts en-
 694 hance carbon export due to gravitational sinking and subduction. *Proceed-
 695 ings of the National Academy of Sciences of the United States of America*,
 696 114(6), 1252–1257. Retrieved from <https://pnas.org/doi/full/10.1073/pnas.1609435114> doi: 10.1073/pnas.1609435114
- 697 Takahashi, T., Sutherland, S. C., Sweeney, C., Poisson, A., Metzl, N., Tilbrook, B.,
 698 ... Nojiri, Y. (2002). Global sea-air CO₂ flux based on climatological sur-
 699 face ocean pCO₂, and seasonal biological and temperature effects. *Deep-Sea
 700 Research Part II: Topical Studies in Oceanography*, 49(9-10), 1601–1622. doi:
 701 10.1016/S0967-0645(02)00003-6
- 702 Taylor, R. (1990). Interpretation of the Correlation Coefficient: A Basic Re-
 703 view. *Journal of Diagnostic Medical Sonography*, 6(1), 35–39. doi:
 704 10.1177/875647939000600106
- 705 Treguier, A. M., Theetten, S., Chassignet, E. P., Penduff, T., Smith, R., Talley,
 706 L., ... Böning, C. (2005). The North Atlantic subpolar gyre in four high-
 707

- resolution models. *Journal of Physical Oceanography*, 35(5), 757–774. doi: 10.1175/JPO2720.1
- Uchida, T., Balwada, D., Abernathey, R., McKinley, G., Smith, S., & Lévy, M. (2019). The Contribution of Submesoscale over Mesoscale Eddy Iron Transport in the Open Southern Ocean. *Journal of Advances in Modeling Earth Systems*, 11(12), 3934–3958. Retrieved from <https://agupubs.onlinelibrary.wiley.com/doi/10.1029/2019MS001805> doi: 10.1029/2019MS001805
- Vic, C., Hascoët, S., Gula, J., Huck, T., & Maes, C. (2022). Oceanic Mesoscale Cyclones Cluster Surface Lagrangian Material. *Geophysical Research Letters*, 49(4), e2021GL097488. Retrieved from <https://agupubs.onlinelibrary.wiley.com/doi/abs/10.1029/2021GL097488> doi: <https://doi.org/10.1029/2021GL097488>
- Wain, D. J., Lilly, J. M., Callaghan, A. H., Yashayaev, I., & Ward, B. (2015, jun). A breaking internal wave in the surface ocean boundary layer. *Journal of Geophysical Research: Oceans*, 120(6), 4151–4161. Retrieved from <https://agupubs.onlinelibrary.wiley.com/doi/10.1002/2014JC010416> doi: 10.1002/2014JC010416
- Wang, L., Gula, J., Collin, J., & Mémery, L. (2022). Effects of Mesoscale Dynamics on the Path of Fast-Sinking Particles to the Deep Ocean: A Modeling Study. *Journal of Geophysical Research: Oceans*, 127(7), e2022JC018799. Retrieved from <https://onlinelibrary.wiley.com/doi/10.1029/2022JC018799> doi: 10.1029/2022JC018799
- Wenegrat, J. O., Thomas, L. N., Sundermeyer, M. A., Taylor, J. R., D'Asaro, E. A., Klymak, J. M., ... Lee, C. M. (2020). Enhanced mixing across the gyre boundary at the Gulf Stream front. *Proceedings of the National Academy of Sciences of the United States of America*, 117(30), 17607–17614. doi: 10.1073/pnas.2005558117